Solar Phys (2015) 290:2093–2116
DOI 10.1007/s11207-015-0720-1

Evolution and Flare Activity of δ-Sunspots in Cycle 23

K. Takizawa[1] · **R. Kitai**[1,2]

Received: 7 October 2014 / Accepted: 2 June 2015 / Published online: 11 August 2015

Abstract The emergence and magnetic evolution of solar active regions (ARs) of $\beta\gamma\delta$-type, which are known to be highly flare-productive, were studied with SOHO/MDI data in Cycle 23. We selected 31 ARs that can be observed from their birth phase as unbiased samples for our study. From the analysis of the magnetic topology (twist and writhe), we obtained the following results: i) Emerging $\beta\gamma\delta$ ARs can be classified into three topological types as quasi-β, writhed, and top-to-top. ii) Of these, the writhed and top-to-top types tend to show high flare activity. iii) As the signs of twist and writhe agree with each other in most cases of the writhed type (12 cases out of 13), we propose a magnetic model in which the emerging flux regions in a $\beta\gamma\delta$ AR are not separated, but are united as a single structure below the solar surface. iv) Almost all the writhed-type ARs have downward knotted structures in the middle part of the magnetic flux tube. This is probably the essential property of $\beta\gamma\delta$ ARs. v) The flare activity of $\beta\gamma\delta$ ARs is highly correlated not only with the sunspot area, but also with the magnetic complexity. vi) We suggest that there is a possible scaling-law between the flare index and the maximum umbral area.

Keywords Active regions · Magnetic fields · Photosphere

1. Introduction

A sunspot group with umbrae of opposite polarity within a single common penumbra is called the δ-sunspot group (Künzel, 1960). It is well known that major flares almost always

---

✉ K. Takizawa
takizawa@kwasan.kyoto-u.ac.jp

R. Kitai
kitai@kwasan.kyoto-u.ac.jp

[1] Kwasan and Hida Observatories, Kyoto University, Yamashina-ku, Kyoto 607-8417, Japan

[2] Bukkyo University, Kita-ku, Kyoto 603-8301, Japan

occur in δ-sunspot groups (Tanaka, 1975; Zirin and Liggett, 1987; Sammis, Tang, and Zirin, 2000). Hence, investigating the formation and evolution of the δ-configuration is the key for understanding the main flare activities.

Zirin and Liggett (1987) classified the formation of δ-spots into three types as follows: i) Emergence of a single complex active region (AR) formed below the surface, *i.e.*, the so-called island δ-spot, ii) emergence of large satellite spots near a larger and older sunspot, and iii) collision of sunspots of opposite polarities from different dipoles. Then Ikhsanov, Marushin, and Ikhsanov (2004), from their morphological study of δ-spots, classified the magnetic topology of collisional interaction between two major emerging flux tubes into three types, namely vertical (top-by-top) collision, lateral (side-by-side) collision, and frontal (foot-by-foot) collision (see also Ikhsanov and Marushin, 2003). Although these researches show a variety of ways of δ-spot formation, they did not give us a detailed physical view of the formation of δ-spots. This is because their classifications were phenomenological.

Successive researches (Kurokawa, 1987; Tanaka, 1991; Leka *et al.*, 1996; van Driel-Gesztelyi *et al.*, 1997; Ishii, Kurokawa, and Takeuchi, 1998; Linton *et al.*, 1999; Fan *et al.*, 1999; López Fuentes *et al.*, 2000) have found several physical characteristics of active δ-spots in that they have strong magnetic shear structures in their magnetic neutral line area and their opposite polarities rotate around each other. These characteristics were interpreted as due to the emergence of a kinked flux rope. Ishii, Kurokawa, and Takeuchi (1998) and Kurokawa, Wang, and Ishii (2002) proposed that the δ-spot is produced by the emergence of a twisted magnetic flux rope whose strong shear produces high flare activities. Poisson *et al.* (2013) suggested that the δ-spot could be due to the emergence of a deformed single tube that has a downward convex structure at its middle part with kinking. Thus the twist and writhe of a magnetic rope are now considered as a key factor for the development of δ-spots and the associated flare activities that sometime show sigmoidal morphology (Rust and Kumar, 1996).

Although a number of case studies revealed the important characteristics of δ-spot evolution, we have not yet had a conclusive observational and physical view of the δ-spot formation. In this article, we tried to obtain more clues on this issue by surveying the δ-spots in solar activity cycle 23 with a focus on magnetic helicity (twist and writhe). Of all the δ-spots in Cycle 23, we selected those that can be studied from their birth on the visible solar disk in order to unambiguously study the magnetic connection between component sunspots in a group. Furthermore, we limited the samples to the $\beta\gamma\delta$ regions, as they show the highest flare activity (Sammis, Tang, and Zirin, 2000). The magnetograms and the continuum images taken with the *Michelson Doppler Imager* (MDI; Scherrer *et al.*, 1995) onboard the *Solar and Heliospheric Observatory* (SOHO; Domingo, Fleck, and Poland, 1995) were used to follow the evolution of the ARs.

Our study shows that the flare-active δ-spots are mainly formed by the emergence of writhed and twisted magnetic tubes, which appear as a quadrupolar magnetic configuration on the photosphere. Even the appearance of a more complex δ-configuration can be interpreted as a modification to this basic configuration. On the other hand, the flare activity is low when the magnetic tubes in the δ-configuration show insignificant writhe or twist.

In Section 2, we describe the data used in our study and the analysis method. In Section 3, we present our detailed analysis of some representative cases and summarize our statistical analysis. Finally, we discuss our results and our conclusions in Sections 4 and 5, respectively.

2. Data and Analysis

2.1. Region Selection

To select $\beta\gamma\delta$ ARs in Cycle 23, we based our study on the following two data catalogs: USAF-MWL (also known as USAF-SOON)[1] and USAF/NOAA sunspot data.[2] The former data base is a compilation of daily solar reports of six ground-based observatories. The latter mainly consists of data based on space observations after the launch of the SOHO spacecraft. When the type of an AR is assigned differently in the two catalogs, we choose the more complex one of the region as the representative. In this way, we selected 200 $\beta\gamma\delta$ regions that are classified so at least once during their lifetime. Four ARs classified as $\beta\gamma\delta$ in the catalogs were excluded from our dataset because they showed no sign of δ-type in our visual check with SOHO/MDI images. Finally, we found and selected 31 candidates that can be studied from their initial emergence on the visible solar disk with reference to the Solar-Monitor website.[3]

2.2. Imaging Data

To follow the evolutions of ARs, we used the longitudinal magnetograms and the continuum images taken with SOHO/MDI with a cadence of 96 min and a pixel size of 2.0″. We used the *Geostationary Operational Environmental Satellite* (GOES) X-ray data to estimate the total flare activity of selected ARs. Full-disk Fe XII 195 Å images of the *Extreme ultraviolet Imaging Telescope* (EIT; Delaboudiniére *et al.*, 1995) onboard SOHO taken with a cadence of 12 min and a pixel size of 2.6″ were used to check coronal structures. The *Transition Region and Coronal Explorer* (TRACE; Handy *et al.*, 1999) images in 195 Å, 1600 Å, and 5000 Å taken with a cadence of approximately 1 min and 0.5″ per pixel were also used when available.

2.3. Image Analysis

2.3.1. Alignment of AR Images

A time series of MDI images of a target AR was aligned by the method proposed by Chae (2001) and Chae *et al.* (2001). We converted original images with a resolution of 2 arcsec into images with one-arcsecond resolution and then applied a nonlinear mapping to remove the differential rotation effect. With these aligned images, we studied the evolution of the target AR and measured the duration of the δ-state by comparing the magnetograms with the continuum images. In this study, we set the brightness levels of 0.9 for penumbrae and 0.65 for umbrae relative to the intensity of the quiet region (see Figure 1).

2.3.2. Circulation

When we closely examined the evolution of an AR, some sunspots exhibited prominent rotation around their centers. We estimated the magnitude of rotation by measuring the

---

[1] ftp://ftp.ngdc.noaa.gov/STP/SOLAR_DATA/SUNSPOT_REGIONS/USAF_MWL.

[2] http://solarscience.msfc.nasa.gov/greenwch.shtml.

[3] http://www.solarmonitor.org/.

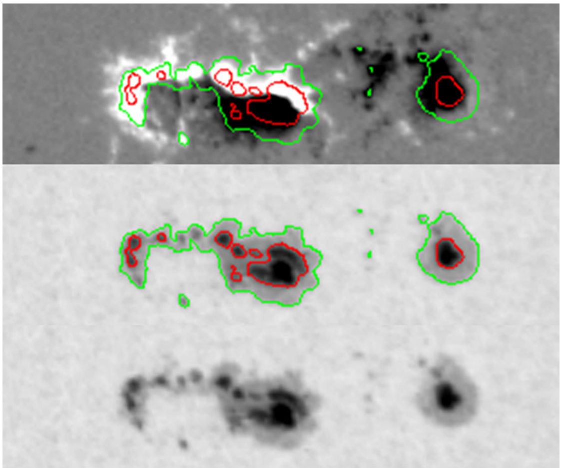

Figure 1 A magnetogram (top panel, gray scale) and a white-light image (bottom panel) of NOAA 10314. Green and red contours show the intensity levels of 0.9 and 0.65 of the quiet region (QR) intensity and delineate QR-penumbra boundaries and penumbra-umbra boundaries, respectively (middle panel). The AR has δ-configuration in the central part.

spatially integrated vorticity around the rotating sunspot in the following manner. First, we realigned the sunspot location in each sequential magnetogram to the center of gravity of the magnetic field strength to remove the effect of proper motion of the sunspot. Second, we applied the local correlation-tracking method (LCT; November and Simon, 1988) to these images to derive the horizontal velocity field ($\mathbf{v}$) around the sunspot. Then, we calculated the area integral of the vorticity, namely circulation (C), by

$$C = \int (\nabla \times \mathbf{v})_z \, \mathrm{d}S, \qquad (\nabla \times \mathbf{v})_z = \frac{\partial v_y}{\partial x} - \frac{\partial v_x}{\partial y}. \tag{1}$$

We trimmed away the edge zone of three-pixel width from the vorticity field to remove fluctuating and erroneous values before the final estimation of the circulation. The trimming was made by first making a binary image from the original vorticity map and then applying the erosion function ERODE in the IDL (Interactive Data Language) software to the binary image, which results in the shrinkage of island areas in the binary image by three pixels, and finally masking the original vorticity map with the eroded binary image. An example of our method for the vorticity field at 17:35 UT on 16 January 2005 is shown in Figure 2. From left to right, we show the velocity field overlaid on the magnetogram, the vorticity field, and the trimmed-away map of the vorticity field. Erroneous vorticity values originate at the border between the real velocity field and the quiet region where the velocity of magnetic features is zero. The erosion operation can eliminate the contaminations from the real rotational elements around the target sunspot effectively, as shown in Figure 2.

According to the mathematical definition of circulation, positive (negative) circulation corresponds to counterclockwise (clockwise) rotation. We note that the signs are opposite to those of the magnetic twist described in Section 2.3.4.

2.3.3. *Tilt Angle of δ-Spots*

The temporal variation of the tilt angle (*i.e.* the inclination angle of the line connecting the bipoles) tells us the orientation of the kink in an emerging magnetic tube. Figure 3 schematically shows the case of a tube with left-handed writhe; upward-kinked (left panel) and downward-kinked (right panel).

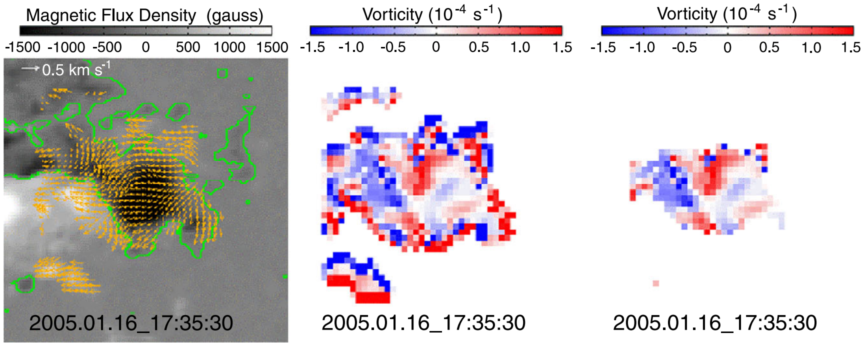

Figure 2 Erosion operation applied to the vorticity field at 17:35 UT on 16 January 2005. From left to right are shown a magnetogram, a vorticity field, and the edge-trimmed map of the vorticity field, respectively. The velocity field (yellow arrows) and neutral lines (green contours) are overlaid on the magnetogram (gray scale).

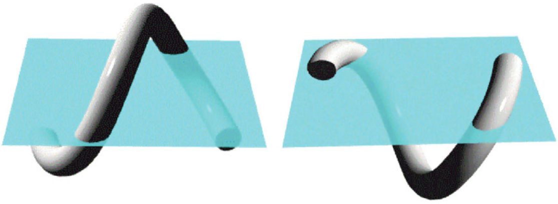

Figure 3 Illustrations of the emergence of tubes with left-handed writhe in the cases of upward-kinked and downward-kinked configurations. In both cases, the inclination angle of the line connecting the two footpoints rotates clockwise, and their separation increases or decreases according to the orientation of the kink.

When they emerge through the photosphere, the tilt angle rotates in the clockwise (CW) direction in both cases. The distance between the footpoints increases for the upward-kinked case, while it decreases for the downward-kinked case. When the tubes with right-handed writhe emerge, the rotation is in the counterclockwise (CCW) direction, and the distance between the footpoints changes according to the kink direction as in the left-handed case. Thus we can infer the orientation of the kink in the emerging magnetic tubes from the temporal variations of the inclination angle and the distance between the two spots.

2.3.4. *Sign of Magnetic Helicity*

A “magnetic tongue” pattern is proposed as a useful parameter to give the sign of magnetic helicity of the emerging field (López Fuentes *et al.*, 2000; López Fuentes and Mandrini, 2008; Luoni *et al.*, 2011). When a twisted tube emerges above the photosphere, the spatial distribution of photospheric magnetic field has an elongated shape like a tongue. The tongues of different polarities show anti-parallel orientations along the neutral line. Since the orientation of a tongue pattern depends on the sense of twist of the emerged tube, we can use this parameter as a proxy of the sign of helicity (twist) of the emerging magnetic tube as shown in Figure 4 (see also Figure 1 of Luoni *et al.*, 2011). The circulation of a sunspot is another measure of the sign of helicity of the magnetic flux tube, and consistency can be checked by comparing these two signs.

To avoid confusion, we here reiterate the definitions for the handedness; the sign of the left (right)-handed twist or writhe is negative (positive), respectively.

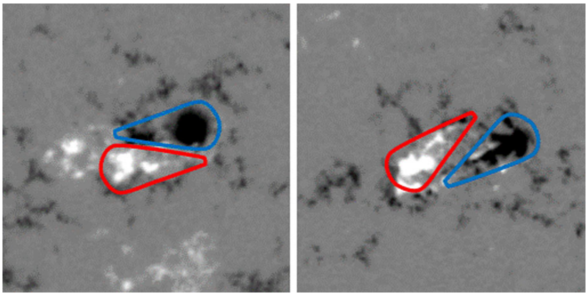

Figure 4 Sample images of magnetic tongues. When the head parts of the Yin–Yang structure forming the magnetic tongues show clockwise or counterclockwise orientation, they indicate negative or positive magnetic helicity, respectively.

2.3.5. Flare Index

Several authors have used the soft X-ray flare index (FI) as a proxy of the activity level of ARs, as given by (*e.g.* Antalová, 1996; Joshi and Joshi, 2004; Abramenko, 2005; Jing *et al.*, 2006)

$$\mathrm{FI} = 1.0 \times \sum_i m_{\mathrm{C}} + 10.0 \times \sum_j m_{\mathrm{M}} + 100.0 \times \sum_k m_{\mathrm{X}}, \tag{2}$$

where m_{C}, m_{M}, and m_{X} are the GOES soft X-ray peak intensity magnitudes (from 1.0 to 9.9) of C, M, and X-class flares. The indices i, j, and k designate flares in each class per unit time period. For an AR, two kinds of periods were considered in this article: those in which the AR was visible on the disk and the AR was in the δ-state. We did not consider flares smaller than C-class in this study because they frequently tend to be hidden by major flares or are indistinguishable from the background level.

3. Results

The δ-spots studied in this article can be classified, from the point of view of the emergence morphology, the magnetic connection, the helicity of sunspots, and the flare activity, into the following groups: i) top-to-top collision, ii) writhed loop, iii) quasi-β, and iv) the others. The majority of δ-spots in our sample are classified into the first three groups. In the next subsection, we select and describe the features of a representative example of each group to show our classification scheme.

3.1. Case Studies

3.1.1. Evolution of NOAA 10720

NOAA 10720 was the most flare-productive region in our samples. It had the longest δ-duration (longer than 213 h) and showed rapid expansion since its emergence.

The magnetic and morphological evolution of the region was as follows: First, an emerging flux region (EFR1) emerged as a simple β magnetic configuration with an almost East–West orientation obeying Hale's law. Then it rapidly expanded in size and evolved to the δ-configuration on 12 January 2005, as shown in Figure 5. Another new highly sheared EFR (EFR2), which disobeyed Hale's law, appeared on the neutral line as if it tried to penetrate the opposite polarity portion of EFR1 at around 16:00 UT on 13 January 2005.

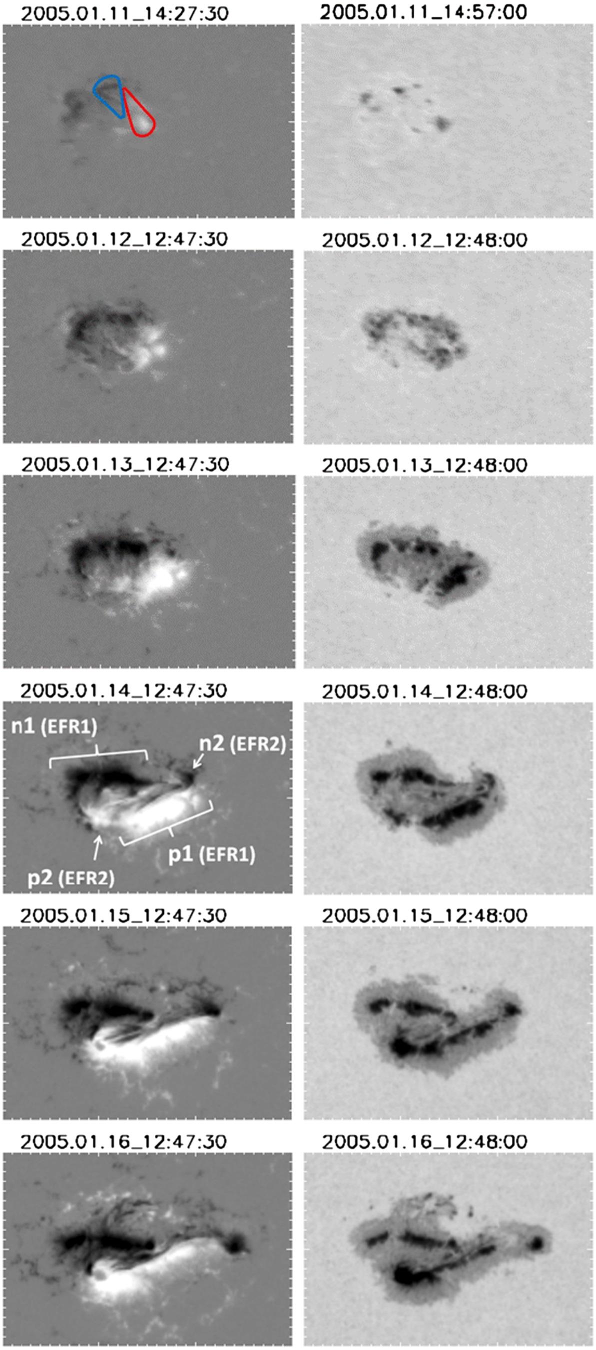

Figure 5 SOHO/MDI magnetograms (left) and white-light images (right) of NOAA 10720 corresponding to subsequent days of observations. The identified two EFRs are shown in the fourth row. The field of view (FOV) of each panel is 300 × 200 arcsec.

In Figure 5, we cannot see any signature of writhe in EFR1, as its tilt showed no systematic rotational movements. The magnetic tongues of EFR1 in the initial emerging phase indicated negative magnetic helicity, as shown in the first row of Figure 5. This means that

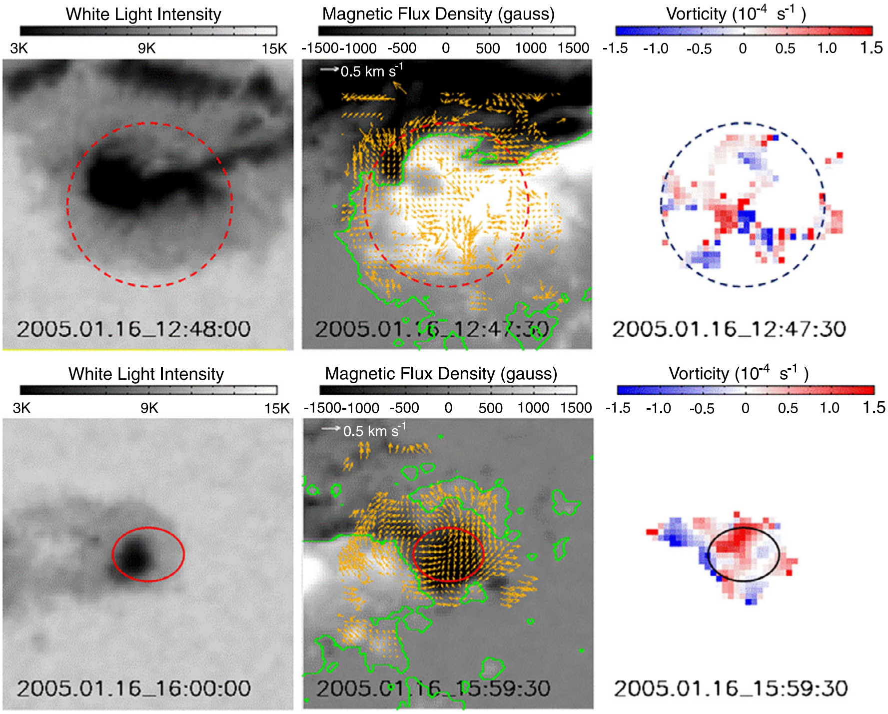

Figure 6 White-light images (left), magnetograms (middle), and vorticity fields (right) of the positive (top row) and negative (bottom row) polarity areas of EFR2, respectively. The size of each FOV is 100 × 100 arcsec, and its center is at the center of gravity of the magnetic flux distribution. In the middle panels the velocity fields (yellow arrows) and the neutral lines (green contours) are overlaid. The areas used to compute the circulation are shown by a circle of 28 arcsec radius in the top row and by an ellipse in the bottom row, whose major and minor axes are 24 and 18 arcsec, respectively.

the tube emerged with a left-handed twist. Unfortunately, the tongue pattern could not be clearly seen after the vigorous and complex development of EFR1.

On the other hand, the tilt angle of EFR2 showed a slow CW rotation, suggesting the emergence of a loop with left-handed writhe. The twist of the magnetic tubes can be estimated by the circulation around the footpoints of the magnetic tubes, *i.e.* sunspots.

Now we consider the distribution of vorticity around the sunspots of p2 and n2 shown in Figure 6. By specifying the integration area with a circle or an ellipse, which covers the target sunspot as compactly as possible, we estimated the circulation over the area covering each sunspot. The reliability of the circulation value was estimated by changing the size of the calculation area. The area was enlarged or reduced by 2 arcsec for this purpose. In addition to the procedures described in Section 2.3.2, we masked the opposite-polarity areas before the integration to avoid contamination. The temporal evolution of the circulation of each sunspot is displayed in Figure 7. Both sunspots showed generally positive circulation, although they showed negative values at times. When we closely examined the vorticity map and the motions of small sunspots in the neighborhood of the n2 spot for a day on 16 January, we found that the rapid sliding motions of small sunspots relative to the static environment were recorded as false negative circulation. If we take this contamination into account, we can assume that the circulations around the p2 and n2 spots were mostly positive during the evolution, which means that the footpoints of the magnetic tube of EFR2

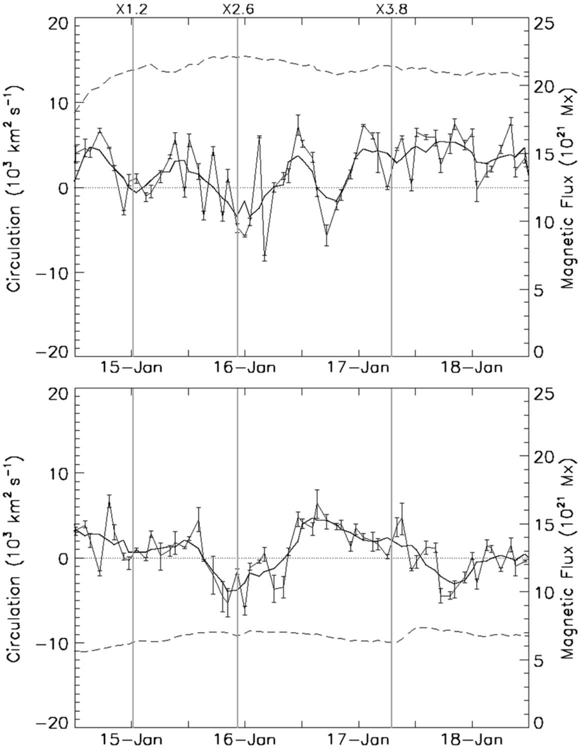

Figure 7 Time variations of circulation (thin solid lines) and magnetic flux (dashed lines) in sunspots p2 (top) and n2 (bottom) in NOAA 10720. The thick solid line shows the running average of the circulation over five consecutive data points in each panel. The error bars indicate a possible range of the circulation values when the size of the analysis area changed (see text). Vertical lines represent the times of the X-class flares. The magnetic flux values are evaluated for the full FOV of Figure 6.

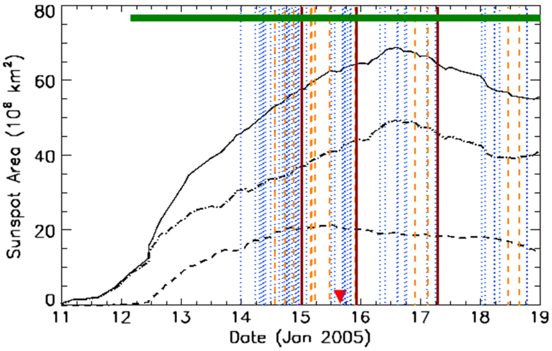

Figure 8 Time evolution of umbra (dashed), penumbra (dash-dotted), and total sunspot (solid) areas in NOAA 10720. Vertical lines indicate X-class (brown solid), M-class (orange dashed), and C-class (blue dotted) flares, respectively. The horizontal thick green line at the top represents the duration of the δ-state. The triangle at the bottom indicates the central meridian passage of the region.

showed a CCW rotation during their evolution. Therefore, EFR2 can be considered as an emerging loop of a left-handed twist.

The timing of the flaring in the region is shown in Figure 8. After the emergence of EFR2 on 13 January, many flares have occurred, including three X-class flares. The high activity triggered by the emergence of EFR2 was reminiscent of the top-to-top collision model proposed by Ikhsanov, Marushin, and Ikhsanov (2004). The flare morphology gave us additional information on the magnetic helicity of EFR2. The SOHO/EIT 195 Å image in the left panel of Figure 9 shows an inverse-S shaped structure over EFR2 after the X1.2 flare that peaked at 0:43 UT. The inverse-S sigmoid morphology indicates the left-handed twist of the

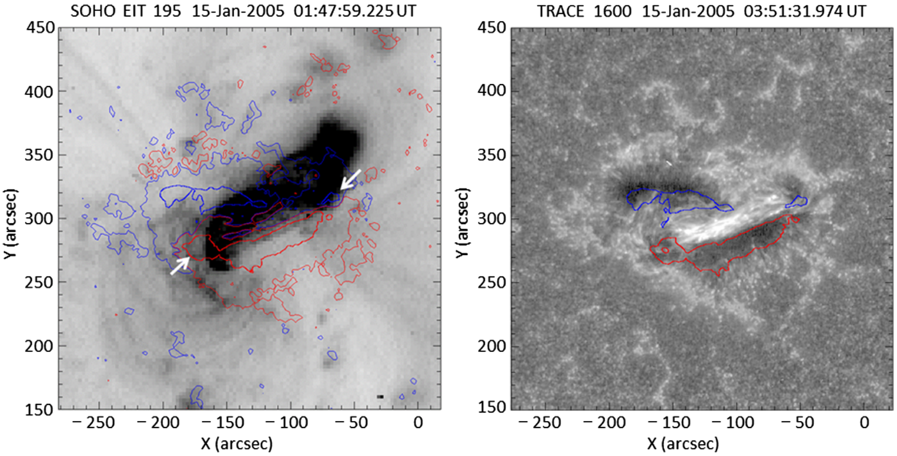

Figure 9 Left: A SOHO/EIT 195 Å image (in negative print) of NOAA 10720 taken at 01:47 UT, 15 January 2005, after the X1.2 flare peaked at 01:02 UT. White arrows indicate two polarities of EFR2. An inverse-S shaped structure is clearly seen. Right: A TRACE 1600 Å image taken at 03:51 UT on 15 January 2005 between the two X-class flares. A bright structure existed between the two polarities of EFR2 even in a relatively quiet period of flare activity. Overlaid contours (red for positive and blue for negative polarities) show the line-of-sight magnetic fields of 1500 gauss (G) and 100 G (only in the left panel). The FOV of both images is 300 × 300 arcsec.

magnetic tube. The TRACE 1600 Å image in the right panel of Figure 9 shows bright loops connecting the two polarities of EFR2. Guo *et al.* (2013) argued that negative helicity was accumulated in EFR2 by a model of nonlinear force-free fields, suggesting the emergence of a tube with a left-handed twist.

Thus, we conclude that the significant flare activity of NOAA 10720 is due to the emergence and the intrusion of the twisted and writhed EFR2 into the magnetic neutral line of the pre-emerged EFR1. This region is a typical example of the top-to-top collision formation of an active δ-type spot.

3.1.2. Evolution of NOAA 10826

A day after the emergence of 29 November 2005, NOAA 10826 formed a δ-configuration and showed high flare activity in the δ-duration of 56 h.

Its magnetic and morphological evolution is shown in Figure 10. Two EFRs emerged in succession along the East–West line. The δ-configuration was formed between the following sunspot of EFR1 and the preceding sunspot of EFR2.

The magnetic tongue patterns of EFR1 and EFR2 showed the sign of negative helicity (the top row of Figure 10), suggesting the emergence of magnetic tubes with a left-handed twist. The tilt of the δ-configuration rotated in the CW direction, with an average rotational speed of $35^\circ\ \mathrm{day}^{-1}$, which is similar to the speed of $30^\circ\ \mathrm{day}^{-1}$ measured in NOAA 10314 by Poisson *et al.* (2013). As the separation between the umbrae of the δ-spot decreased in the first stage, this δ-configuration behaved as the emergence of a tube with left-handed writhe and downward kink. As the twist had the same sign as the writhe, we suggest that the tube was kinked downward as a result of the transformation into the writhe from the twist in the layers below the photosphere.

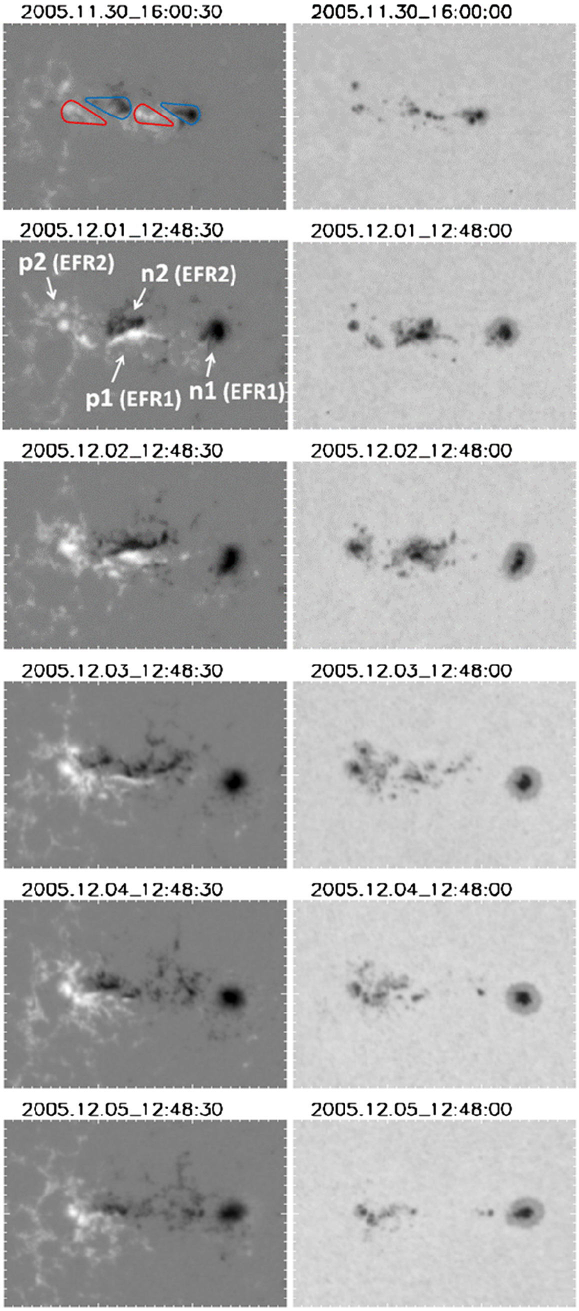

Figure 10 SOHO/MDI magnetograms (left) and white-light images (right) of NOAA 10826. The two identified EFRs are shown in the second row. The FOV of each panel is 300 × 200 arcsec.

We studied the magnetic twist of EFR1 and EFR2 by examining the circulation at the footpoints of EFRs. We selected sunspots n1 of EFR1 and p2 of EFR2 for the evaluation of circulation, as they were isolated and free from possible contamination. From the temporal variations of circulation shown in Figure 11, we conclude that the circulations in both

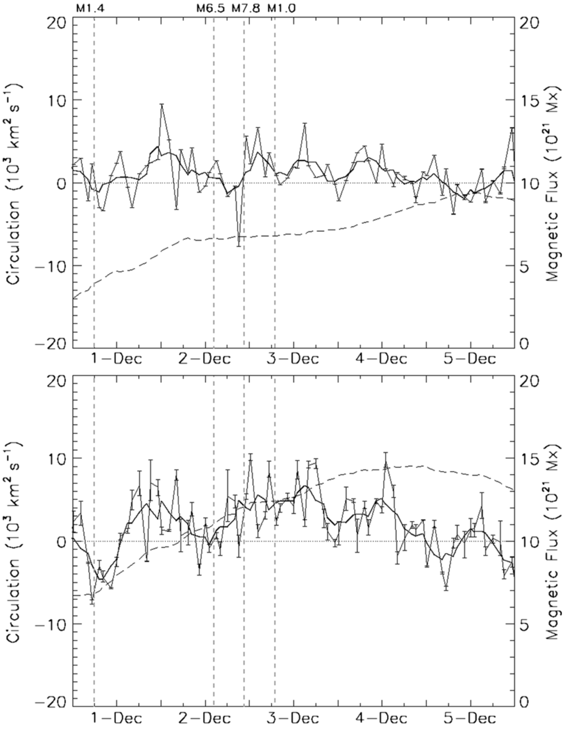

Figure 11 Time variations of circulation (thin solid lines) and magnetic flux (dashed lines) in sunspots n1 (top) and p2 (bottom) in NOAA 10826. The format is the same as in Figure 7.

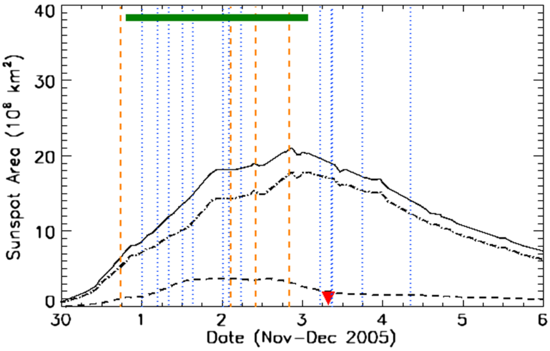

Figure 12 Time evolution of umbra (dashed), penumbra (dash-dotted), and total sunspot (solid) areas in NOAA 10826. The format is the same as in Figure 8.

sunspots were predominantly positive, which means that the sunspots in the two EFRs rotated in the CCW direction, *i.e.* the tubes emerged with a left-handed twist.

High flare activity in this region started just after the formation of the δ-configuration, producing 17 flares in total (4 M-class and 13 C-class) during its disk passage and 11 flares (3 M-class and 8 C-class) during the δ-configuration (Figure 12). The flare morphology gave some insight on the topology near the neutral line of the δ-configuration. Figure 13 shows the case of an M1.0 flare. We can see that the bright flare strand had a highly sheared structure with a left-handed twist. Since the bright strand was probably produced by the magnetic reconnection in the corona, we can infer that the magnetic field near the neutral line had left-handed helicity before the flare explosion.

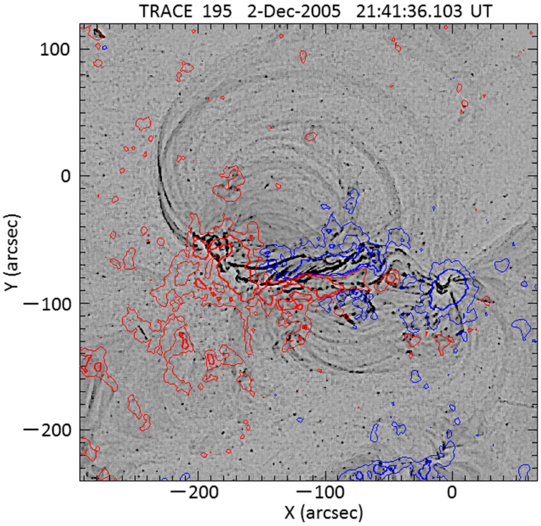

Figure 13 A high-pass filtered TRACE 195 Å image (in negative print) of NOAA 10826. Contours indicate line-of-sight magnetic fields of 500 G (thick) and 100 G (thin) in positive (red) and negative (blue) polarity areas. After the M1.0 flare, highly sheared bright structures appeared on the δ-part of the region.

All the direct or indirect evidence indicates that the EFRs in this region had the same left-handed helicity. As the magnetic fluxes of sunspots n1 and p2 were on the same order of magnitude (Figure 11), it is natural to assume that the two EFRs were not physically separated but connected like a single writhed structure as in the case of NOAA 10314 reported by Poisson *et al.* (2013). Therefore we classify this region as of the "downward knotted" type.

3.1.3. Evolution of AR NOAA 10050

NOAA 10050 emerged on 26 July 2002. Although the region developed due to successive emergence of several EFRs, flare activity was low. A few δ-configurations formed and disappeared within their lifetime of less than a day at different locations in the region. See Figure 14 for the magnetic and morphological evolution of the region.

The EFRs in the region emerged with their axes in the East–West direction. As they evolved, the two opposite polarities of each EFR were separated from each other, and sunspots of each polarity merged into a dominant center. The evolution was very similar to the bipolar emergence model of Zwaan (1978). The δ-configuration formed transiently when a pair of small opposite-polarity elements incidentally came together. We found no signature of writhe pattern in their motion.

The temporal evolutions of circulation around the dominant polarities are shown in Figure 15. The preceding negative polarity significantly changed its circulation from negative to positive in the early phase of the evolution. After several changes in its sign, the positive circulation became dominant in the later phase. On the other hand, the following positive polarity always indicated negative circulation during the period. The circulations of the two polarities had a tendency to show opposite directions. Furthermore, the evolution of circulation was strongly influenced by the successive merging of small sunspots. Therefore, we may conclude that the actual twist of the dominant sunspots was low. The flare activity in the δ-state of this region was very modest, as shown in Figure 16.

The evolution of the region is very similar to the β-type, and we classify the region as of the "quasi-β" type.

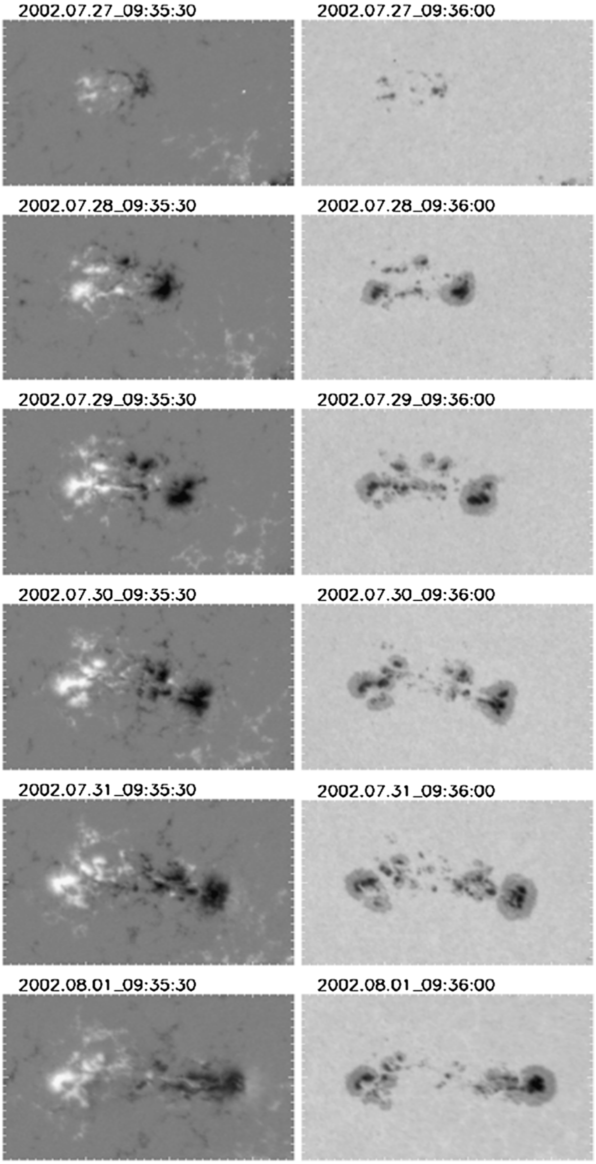

Figure 14 SOHO/MDI magnetograms (left) and white-light images (right) of NOAA 10050. The FOV of each panel is 350 × 200 arcsec.

3.2. Statistical Study

In our case studies of δ-spots, we noted high flare activity in magnetically complex δ-spots. In this subsection, we statistically analyze the dependence of the flare activity on the characteristic parameters of δ-spot regions.

3.2.1. Parameters

In Table 1, we summarize several flare indices and the parameters that characterize the 31 ARs we studied. The peak soft X-ray flux ($\mathrm{XR_{max}}$) and FI are the flare indices, while

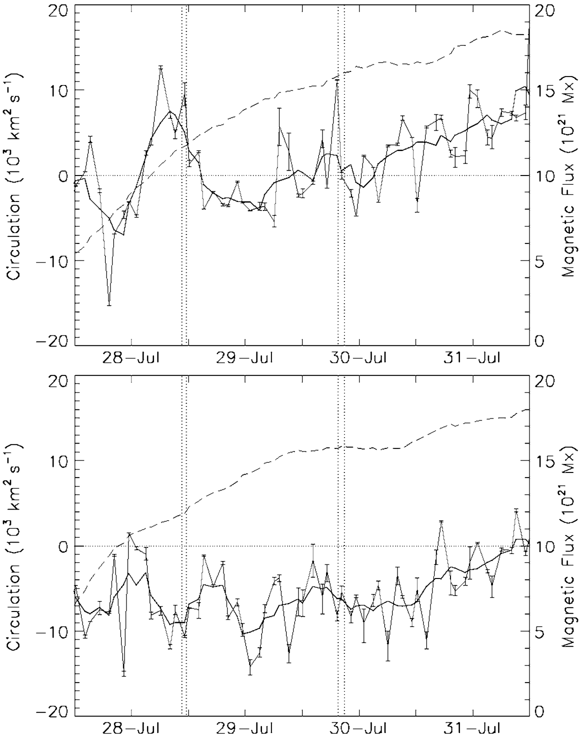

Figure 15 Time variations of circulation (thin solid lines) and magnetic flux (dashed lines) in the preceding negative-polarity sunspot (top) and the following positive-polarity sunspot (bottom) in NOAA 10050. The format is the same as in Figure 11. Dotted vertical lines represent C-class flares.

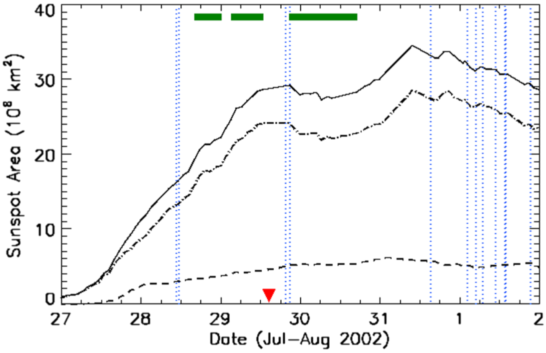

Figure 16 Time evolution of umbra (dashed), penumbra (dash-dotted), and total sunspot (solid) areas in NOAA 10050. The format is the same as in Figure 8.

the maximum sunspot area ($S_{\max}$), the maximum umbral area (S_{Umax}), δ-term (the duration of the δ-state), the handedness of twist and writhe, and the type of δ-spot formation are the characteristic parameters of ARs. We comment on the values of these parameters in the following paragraphs.

An AR develops and changes its magnetic type and sometimes passes through the West limb while keeping its high activity. To eliminate possible ambiguity and uncertainty in the estimated parameters, we only considered the events that occurred in longitudes lower than W70°. The values of FI were thus counted and listed in Table 1. The values in parentheses are for the flares that occurred during the δ-state of the region. The identification of the δ-state was also limited to longitudes lower than W70°, so that it gives a lower limit in some cases.

Table 1 Summary of parameters for 31 ARs. The upper part of the table is for ARs in the northern hemisphere, while the lower part is for those in the southern hemisphere. Here, $\mathrm{XR}_{\max}$ means the peak X-ray flux in the observed period of each AR. Flare Index indicates the value integrated over the observed period (the value integrated over the δ-state is shown in parentheses). $S_{\max}$ means the maximum sunspot area in the observed period. S_{Umax} means the maximum umbral area in the observed period (the value in the δ-state is shown in parentheses). δ-term shows the integrated duration of the δ-state. The twist and writhe are indicated by R (right-handed) or L (left-handed). The "Type" column shows the emergence type of ARs; TT (top-to-top), DK (downward knotted), UK (upward knotted), and QB (quasi-β), respectively.

AR	$\mathrm{XR}_{\max}$ (Wm^{-2})	Flare index	$S_{\max}$ (Mm^2)	S_{Umax} (Mm^2)	δ-term (h)	Twist	Writhe	Type
9165	59.0	257.0 (42.2)	1851	291 (280)	24	L	L	UK
9511	120.0	275.9 (247.5)	714	114 (114)	20	R	R	DK
9678	20.0	103.1 (40.3)	3046	623 (584)	26	L to R	L	DK
9901	40.0	53.1 (53.1)	2003	283 (283)	188	–	R	–
10412	9.8	22.8 (6.0)	944	170 (160)	27	R	R	DK
10488	19.0	191.8 (191.8)	6786	1789 (1789)	158	L	L	DK
10564	110.0	219.0 (209.0)	3716	659 (659)	110	–	–	TT
10696	250.0	1114.9 (1062.1)	3841	829 (829)	192	L	L	TT
10720	710.0	2299.3 (2299.3)	6906	2147 (2147)	213	L	L	TT
10956	2.9	3.9 (2.9)	1054	151 (151)	112	–	–	–
8506	3.3	9.1 (0.0)	1285	245 (211)	8	R	–	QB
8926	2.3	96.6 (41.6)	805	152 (152)	52	L	L	DK
9494	10.0	59.9 (26.7)	1105	251 (159)	32	R	R	DK
9775	22.0	115.3 (11.0)	1415	144 (144)	32	L	L	DK
9900	4.4	11.2 (0.0)	633	75 (67)	10	–	–	–
9904	9.2	8.2 (0.0)	247	52 (52)	30	–	L	–
9906	26.0	58.1 (48.5)	2907	540 (540)	114	R	R	DK
10017	150.0	282.5 (174.4)	2298	341 (341)	34	R	R	TT
10050	8.6	57.5 (6.5)	3408	627 (600)	38	–	–	QB
10119	8.8	54.9 (14.0)	3192	541 (541)	92	L	–	QB
10137	40.0	174.7 (170.0)	1330	252 (252)	88	L	L	DK
10226	68.0	231.6 (124.0)	2812	578 (578)	110	L	R	DK
10314	150.0	511.1 (443.9)	2367	635 (635)	94	R to L	R	DK
10417	5.2	39.7 (6.9)	1405	199 (158)	15	–	–	QB
10456	4.4	6.6 (2.2)	772	101 (60)	14	–	–	QB
10551	3.2	6.9 (0.0)	1531	221 (221)	38	–	–	QB
10591	12.0	12.0 (12.0)	412	82 (82)	32	R	–	–
10798	56.0	84.8 (84.3)	2931	461 (461)	65	R	–	TT
10826	78.0	204.7 (200.9)	2152	390 (390)	56	L	L	DK
10848	41.0	14.9 (0.0)	1466	181 (181)	21	–	–	–
10865	14.0	30.0 (0.0)	2532	568 (285)	38	–	–	QB

The δ-state in an AR sometimes varied in time. If there appeared multiple δ-states intermittently in an AR, we summed all the time spans of δ-periods to obtain the δ-duration (or δ-term) in this study. When there was a gap longer than several hours in the available

MDI continuum images, we also used TRACE white-light images to estimate the δ-duration. However, there remains an uncertainty ranging from 7 h to 31 h, which is regarded as the estimation error for the δ-duration.

As seen in our case studies, the magnetic field distributions in $\beta\gamma\delta$ ARs are complex, and the estimation of the magnetic twist from the circulation is sometimes ambiguous. However, it is well known that the preceding sunspots have a more rigid structure and longer lifetime than the following sunspots (van Driel-Gesztelyi and Petrovay, 1990), while the following sunspots tend to be affected by turbulent motions in the surroundings, which cause the fragmentation of the flux tube (Fan, Fisher, and Deluca, 1993). Therefore we mainly measured the circulation of the preceding sunspots and adopted their handedness of twist as more reliable representatives of the ARs. To decide the sign of writhe, we considered the evolution of the δ-part as described in Section 2.3.3.

The flare that corresponded to the peak X-ray flux only represents a single event of an AR, although the observational period and the event did not always occur in the δ-state. On the other hand, FI can be measured over the definite period of the δ-duration. Therefore, we regarded FI as a better parameter of flare activity in the δ-state than $\mathrm{XR}_{\mathrm{max}}$.

3.2.2. Flare Activity and Sunspot Area

Sammis, Tang, and Zirin (2000) statistically studied the relation between the flare activity and the maximum sunspot area for the ARs in Cycle 22 and found that ARs with a larger maximum sunspot area produced higher peak X-ray flux. They showed in particular that $\beta\gamma\delta$-ARs had the largest maximum sunspot area and hence produced the strongest flares. We now investigate the relation between the FI (the proxy of flare activity level) and the maximum umbral area for our sampled $\beta\gamma\delta$-ARs in Cycle 23.

First, we confirm that the relation found by Sammis, Tang, and Zirin (2000) also holds in our data. The physical meaning of the relation is that the sunspot area is a measure of the total magnetic flux of the region and hence represents the magnetic energy content of the region. The ARs with a high content of magnetic energy can produce a strong release of energy as flaring. As we do not have the magnetic flux values for all the ARs in Cycle 23, we have to use the measured area as a proxy parameter for the magnetic flux. The line-of-sight magnetic data by SOHO, for example, cannot provide a reliable estimate of the magnetic flux, without correcting for the projection effect and the field inclination to the vertical. We took the umbral area as a better proxy parameter of the magnetic flux than the total sunspot area including the penumbral area because of two reasons. The first is that larger sunspots have smaller ratio of penumbra to the total sunspot area (left panel of Figure 17) and contain more magnetic flux in the umbral area (Antalová, 1991; Jin *et al.*, 2006). The other empirical reason is that FI does not depend so strongly on the penumbra-umbra radius ratio when this ratio is high (right panel of Figure 17).

Next, we note the large dispersion in FI in Figure 18. For a given maximum umbral area, there appears to be a variety of ARs from highly flare productive ones to less productive ones. In Figure 18, $\beta\gamma\delta$ ARs are roughly split into different emergence types, suggesting that the emergence mode is another key parameter to characterize the flare productivity. By comparing the two panels in the figure, we can see that the separation of the three groups in the right panel is clearer than in the left panel. Since the clear separation into groups may give indications of the δ-state, we below mainly concentrate on the flare activity and the area variation in the δ-state.

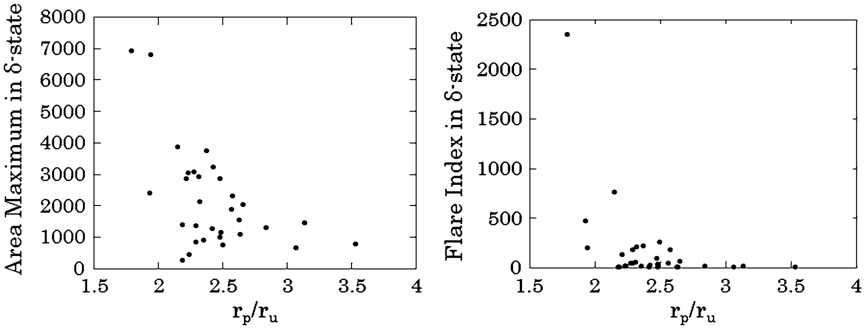

Figure 17 $S_{\max}$ (left) and FI (right) *versus* the penumbral-umbral radius ratio in the δ-state.

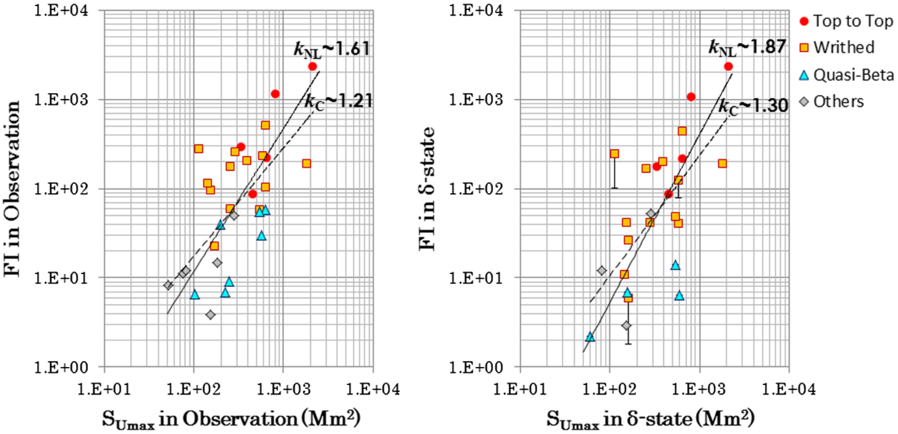

Figure 18 Flare index *versus* maximum umbral area on a logarithmic scale. The left panel shows the data in the observed period and the right panel those in the δ-state. Six ARs that showed no flare activity in the δ-state were excluded. Different symbols indicate top-to-top (red circles), writhed (orange squares, both DK and UK types in Table 1), quasi-β (blue triangles), and others (gray diamonds), respectively. The error bars were assigned by considering the effect of data gaps (see text). The results of nonlinear least-squares fitting (power-law index k_{NL}) and classical least-squares fitting (power-law index k_{C}) are shown as solid and dashed lines, respectively.

3.2.3. *Flare Activity and Emergence Type*

Figure 19 shows the histogram of S_{Umax} and FI distributions grouped according to the emergence type in the δ-state. We combined the groups DK (downward-kinked) and UK (upward-kinked) in Table 1 as the writhed type. The bin sizes of S_{Umax} and FI are $10^{0.4}$ (≈ 2.51) and $10^{0.7}$ (≈ 5.01), respectively. The grouping follows the decreasing order of magnetic complexity (*i.e.* top-to-top, writhed, quasi-β, and others). As the topological complexity decreases, both S_{Umax} and FI distribute to lower values. The relation found here clearly indicates that the flare activity of $\beta\gamma\delta$ ARs depends not only on the umbral area, but also on the magnetic complexity. Moreover, it suggests that the large total content of magnetic flux represented by the umbral area is a necessary condition, and significant magnetic complexity may be another more stringent necessary condition for the activation of strong flares.

Figure 19 Histograms of umbral area maximum (left) and FI (right) in the δ-state period. From the second row downward we show top-to-top, writhed, quasi-β, and others types, respectively, and the top row shows the total.

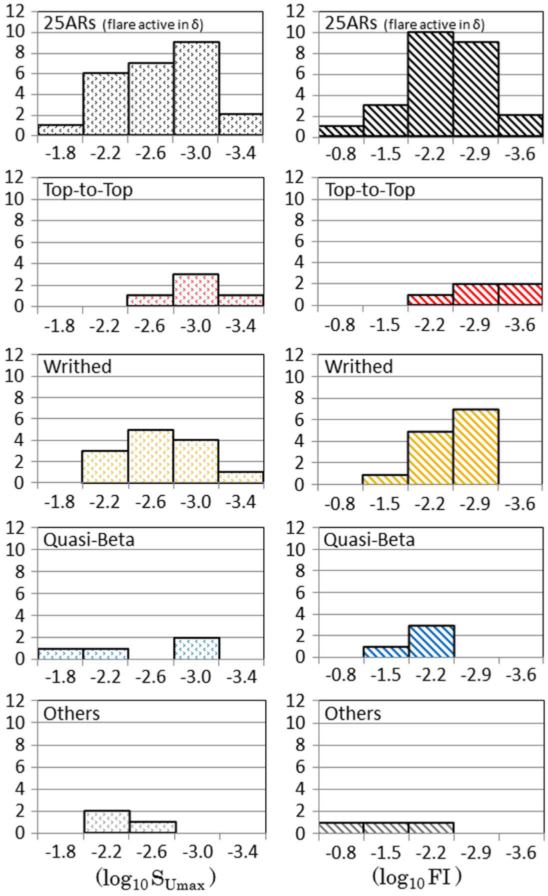

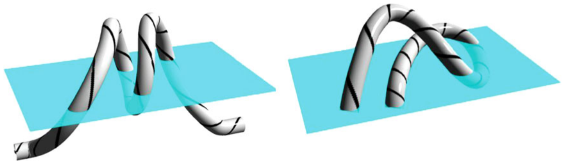

Figure 20 Schematic models for $\beta\gamma\delta$ ARs. The left panel shows a general model for the downward-knotted type such as NOAA 10826. The right panel shows a possible model for the top-to-top type such as NOAA 10720.

3.2.4. *Twist and Writhe of δ-Spots*

When we classified the 31 ARs by their emergence mode, we found 5 ARs to be top-to-top, 13 to be writhed, 7 to be quasi-β, and 6 to be others. Although the quasi-β and others groups hardly ever showed the signs of twist and writhe, the top-to-top and writhed ARs clearly showed the twist and writhe. In most cases of the writhed type, the signs of twist and writhe agree with each other at least in their initial phase (12 cases out of 13). This result strongly suggests that the formation of the δ-spot is not due to the gathering of disjointed EFRs, but to the emergence of a singly connected structure (left panel in Figure 20). The

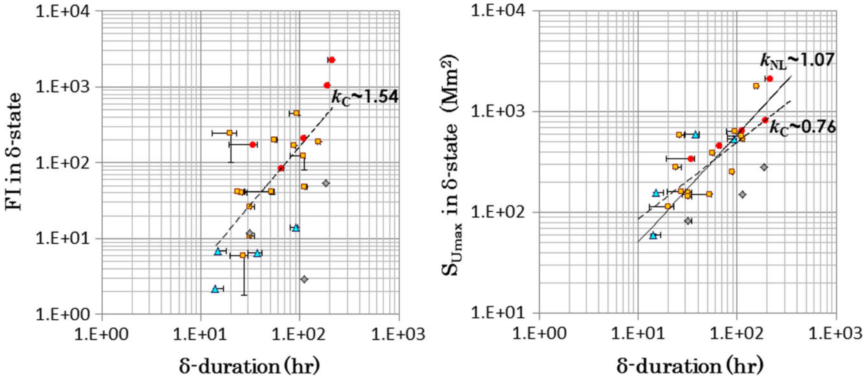

Figure 21 Flare index (left) and maximum umbral area (right) in the δ-state as a function of the δ-duration. The symbols are the same as in Figure 18. Six ARs without flare activity in the δ-state were excluded. The error bars were assigned by considering the effect of data gaps (see text). The results of nonlinear least-squares fitting (power-law index k_{NL}) and classical least-squares fitting (power-law index k_{C}) are shown as solid and dashed lines, respectively.

top-to-top ARs also show a high probability of agreement in their helicity signs (three cases out of five). We speculate that the top-to-top type has a more developed writhing structure than the writhed type (right panel of Figure 20). However, according to the study of Park, Moon, and Gopalswamy (2012), some top-to-top ARs may be associated with the injection of opposite-sign helicities through flux emergence. Therefore the model of top-to-top ARs is at present controversial, and further investigation is necessary to finalize the model.

The majority of writhed ARs were of DK type (12 cases out of 13). The UK type was quite rare. The dominance of DK seems natural because a simple writhed magnetic tube with upward kink will emerge through the photosphere as a normal β-type magnetic distribution and will rarely be identified as the δ-type sunspots.

3.2.5. δ-Duration and Emergence Type

As shown in the left panel of Figure 21, more magnetically complex ARs have longer δ-duration. We already confirmed that more magnetically complex ARs have a larger maximum umbral area in Figure 18.

In general, larger sunspots have a longer lifetime (Gnevyshev, 1938; Waldmeier, 1955). Recurrent sunspot groups are found to exhibit a slightly longer lifetime than that based on the Gnevyshev–Waldmeier relationship by Petrovay and van Driel-Gesztelyi (1997). It is also well known that larger sunspots tend to be darker and have stronger magnetic fields (Solanki, 2002; Livingston, 2002). Furthermore, Shi and Wang (1994) reported that the productivity of δ-spots for X-class flares is closely correlated to the lifetime of δ-spots. Our result suggests that the long lifetime of active δ-spots is closely related to their magnetic complexity (twist and writhe). Although magnetic tubes are eventually dispersed by the action of turbulent convection (Petrovay and Moreno-Insertis, 1997) and/or fragmentation by fluting instabilities, the twisted tubes are more resistant against these dissolving actions. It seems difficult to imagine that the magnetic lines of force of the tube above the solar surface will be torn off by convective motions in lower layers because the lines of force are entangled and hooked to the magnetic tube in the corona. Furthermore, the twist will suppress the fluting instability of magnetic tubes (Priest, 2014). We therefore argue that the longevity of an active δ-spot depends on its magnetic twist.

3.2.6. Possible Power-Law Relations Among Parameters

On every scatter plot (Figures 18 and 21), we performed the power-law fitting to the data. Two methods were used to derive the power-law index k. The first is the classical least-squares fitting (C-LS) to log-log plots, and we obtain the power-law index k_{C}. The second is the nonlinear least-squares fitting (NL-LS) method based on the Gauss–Newton algorithm (*cf.* Hansen, Pereyra, and Scherer, 2012), leading to k_{NL}. For the data points in the left panel of Figure 18 (S_{Umax} *vs.* FI in the observed period), we found $k_{\mathrm{C}} = 1.21 \pm 0.24$ and $k_{\mathrm{NL}} = 1.61 \pm 0.33$. In the right panel of Figure 18 (S_{Umax} *vs.* FI in the δ-state), we found $k_{\mathrm{C}} = 1.30 \pm 0.31$ and $k_{\mathrm{NL}} = 1.87 \pm 0.50$. FI follows a power-law dependence on S_{Umax} with an index of about 2, especially in the δ-state. It is worthwhile to note that Magara (2014) discussed a power-law relationship between the magnetic free energy and the total magnetic flux for twisted emerging loops with an index of 2 from his numerical simulation.

We next show the relation between the δ-duration and FI in the δ-state (left panel of Figure 21). Although we were unable to obtain the converged solution of NL-LS, we obtained $k_{\mathrm{C}} = 1.54 \pm 0.34$ when we excluded the others group, because they have a large dispersion. For the relation between the δ-duration and S_{Umax} in the δ-state (right panel of Figure 21), we found $k_{\mathrm{C}} = 0.76 \pm 0.16$ and $k_{\mathrm{NL}} = 1.07 \pm 0.28$. By combining the last two relations, namely both plots of Figure 21, we can infer a power-law relation FI $\sim S_{\mathrm{Umax}}^{2.0}$ from C-LS that is consistent with the result derived in the previous paragraph.

4. Discussion

By examining the initial phase of $\beta\gamma\delta$ ARs in Cycle 23, we investigated the important configurations that lead to flare activity. From our investigation, we discovered three representative topological types that are strongly correlated with flare activity, namely quasi-β,writhed, and top-to-top. We confirmed that the ARs with higher topological complexity show stronger flare activity.

It is interesting to note that almost all ARs classified as the writhed type are of DK type. Once the downward knot structure is formed, a dense plasma reservoir is formed in the knot, and the whole structure of the flux tube may become stable owing to the effect of the mass as an anchor (left panel of Figure 20). In a different situation, Magara and Longcope (2003) proposed a similar idea in their numerical simulation of the emergence of a twisted flux tube in the convection zone. Subsequently, Magara (2011) has studied the case of the emergence of a U-loop formed below the photosphere. van Driel-Gesztelyi, Malherbe, and Démoulin (2000) have reported the emergence of a U-loop that connected the opposite-polarity legs of two Ω-loops below the photosphere. Recently, Poisson *et al.* (2013) studied the possibility of a downward-kinked structure in the middle part of NOAA 10314. Thus the idea of DK structure is not exceptional and is applicable to twisted magnetic tubes, with several incidences. The DK structure as an anchor may contribute to the stability of the AR.

We also checked the case of the top-to-top group. They show clear twist and writhe structures with common handedness (three cases out of five). From this we infer that the three-dimensional collision is not accidental, but is attributed to the extreme development of a writhing structure. For example, NOAA 10696, classified as of top-to-top type, had the second strongest FI in our sampled ARs and showed characteristics of both three-dimensional collision and downward-knotted structure. The AR is a hybrid type of writhed and top-to-top. The configuration of this AR indicates that there may be a continuing development between the top-to-top and writhed structures. We propose a schematic model for NOAA 10720 with a highly writhed structure as shown in Figure 20 (right panel). A similar, highly writhed model for NOAA 7926 was proposed by Pevtsov and Longcope (1998).

Brown *et al.* (2003) studied the rotation of seven sunspots using high-resolution white-light images with TRACE. They proposed that one possible mechanism for sunspot rotation is the emergence of a pre-twisted flux tube. On the other hand, Yan *et al.* (2009) claimed that the rotation of sunspots originates from the photospheric flows, based on their study of combined photospheric and coronal observations. In our study, the rotation of sunspots themselves and the tilt-angle rotation of EFR are rarely observed in small and flare-inactive ARs. If the rotation is mainly attributed to photospheric flows, rotational motions of sunspots will be observed commonly, regardless of the sunspot size. However, as shown in our statistical study, the ARs of prominent twist and writhe had a larger area and showed stronger flare activity among the sampled ARs. In addition, as described in Section 3.2.5, the pre-twisted flux tube model is in harmony with several features of δ-spots. We therefore conclude that the origin of sunspot rotation is the emergence of the pre-twisted flux tube.

It is known that twist and writhe helicities transform each other in an ideal thin flux tube (Călugăreanu, 1959; Moffatt and Ricca, 1992; Ricca, 1995; Török, Berger, and Kliem, 2010). In this study, we adopted a picture in which the initial twist of ARs will be mostly generated by turbulent flows in the convection zone. When the twist increases in an AR, the twist transforms into the writhe in the middle part of the flux tube by the kink instability (Török, Berger, and Kliem, 2010). Then it is natural to find the sign relationship as seen in this study. Previous studies have shown that the kink instability facilitates the formation of δ-spots (*e.g.* Linton *et al.*, 1999). Tian *et al.* (2005) pointed out that the signs of twist and writhe tend to agree in well-developed ARs under kink instability.

Regarding the classification of δ-spots, we reviewed the relations between the types classified by our study and the types by Zirin and Liggett (1987) as introduced in Section 1. The first type of Zirin and Liggett (ZL) is the same as the top-to-top type we described. The third type of ZL may be equal to the writhed group, although the configuration is probably not formed by different dipoles, but by a connected structure below the photosphere. However, the second type of ZL was seldom observed in our study. This type was seen in only one or two cases in the others group of our study. This type may be more likely to occur in recurrent sunspots instead of in sunspots in their young stage studied here. The quasi-β type was not considered in the ZL classification because they may not produce notable flares.

We discussed the possible power-law relations among the $\beta\gamma\delta$-spot parameters. Our physical interpretation is as follows: FI is a good proxy of the total energy released in flares in an AR and thus is a measure of the total magnetic free energy of the region that is supplied by the gas flow field. The maximum umbral area S_{Umax} is a measure of the magnetic flux of the region. The functional relation of a power law is sometimes interpreted as evidence of a scale-free process (Shimizu, 1995; Shimojo and Shibata, 1999; Nishizuka *et al.*, 2009). In our case, the total free-energy supply or injection can be considered as due to a kind of scale-free processes, probably the helicity injection process by the turbulent convective flows or differential rotation. The process seems to work independent of the total amount of magnetic flux. The difference in FI among the emergence-type groups may be the difference in topology of the magnetic tubes. While the quasi-β type may have a simple form with less twist and less free-energy, the writhed type may have a singly knotted or kinked tube with more free energy, and the top-to-top type may have a doubly or multiply knotted tube with much more free energy.

5. Conclusions

We have studied the initial evolution of 31 $\beta\gamma\delta$ ARs and derived the following conclusions:

i) From the point of view of topology, emerging $\beta\gamma\delta$ ARs can be classified broadly into three categories: quasi-β, writhed, and top-to-top. The top-to-top type has the most complex topology, and the quasi-β type is the simplest type. The writhed group has a medium complexity among the three types.
ii) ARs of more complex topology tend to exhibit higher flare activity.
iii) The signs of twist and writhe both tend to be consistent with each other in the writhed type.
iv) The downward-knotted structure in the middle part of the flux tube is the essential element of active $\beta\gamma\delta$ ARs.
v) The flare activity of $\beta\gamma\delta$ ARs are highly correlated not only with the sunspot areas, but also with the magnetic complexity.
vi) There is a possible scaling-law between FI and S_{Umax}.

Finally, we comment on a future extension of our study. Direct measurements of magnetic helicity are essential to study the free-energy accumulation in ARs. Observations of the ARs throughout their lifetime along with stereoscopic views from space are desirable. Furthermore, it will be an important challenge to diagnose the magnetic topology of ARs in the convection zone by improving local helioseismology.

Acknowledgements The authors appreciate useful comments from an anonymous referee. We thank the SOHO, TRACE, and GOES consortia for their data. SOHO is an international cooperation between ESA and NASA. We are grateful to the staff of Kwasan and Hida observatories of Kyoto University for their continuing help. We wish to thank Hiroki Kurokawa and Yin Zhang for useful discussion. This work was supported by the Grant-in-Aid for the Global COE Program "The Next Generation of Physics, Spun from Universality and Emergence" from the Ministry of Education, Culture, Sports, Science and Technology (MEXT) of Japan. We are partially supported by the grant-in-aid from the Japanese MEXT (PI: R. Kitai No. 26400235).

References

Abramenko, V.I.: 2005, *Astrophys. J.* **629**, 1141. ADS. DOI.
Antalová, A.: 1991, *Bull. Astron. Inst. Czechoslov.* **42**, 316. ADS.
Antalová, A.: 1996, *Contrib. Astron. Obs. Skalnate Pleso* **26**, 98. ADS.
Brown, D.S., Nightingale, R.W., Alexander, D., Schrijver, C.J., Metcalf, T.R., Shine, R.A., Title, A.M., Wolfson, C.J.: 2003, *Solar Phys.* **216**, 79. ADS. DOI.
Călugăreanu, G.: 1959, *Rev. Roum. Math. Pures Appl.* **4**, 5.
Chae, J.: 2001, *Astrophys. J.* **560**, 95. ADS. DOI.
Chae, J., Wang, H., Qiu, J., Goode, P.R., Strous, L., Yun, H.S.: 2001, *Astrophys. J.* **560**, 476. ADS. DOI.
Delaboudiniére, J.-P., Artzner, G.E., Brunaud, J., Gabriel, A.H., Hochedez, J.F., Millier, F., *et al.*: 1995, *Solar Phys.* **162**, 291. ADS. DOI.
Domingo, V., Fleck, B., Poland, A.I.: 1995, *Solar Phys.* **162**, 1. ADS. DOI.
Fan, Y., Fisher, G.H., Deluca, E.E.: 1993, *Astrophys. J.* **405**, 390. ADS. DOI.
Fan, Y., Zweibel, E.G., Linton, M.G., Fisher, G.H.: 1999, *Astrophys. J.* **521**, 460. ADS. DOI.
Gnevyshev, M.N.: 1938, *Pulkovo Obs. Circ.* **24**, 37.
Guo, Y., Ding, M.D., Cheng, X., Zhao, J., Pariat, E.: 2013, *Astrophys. J.* **779**, 157. ADS. DOI.
Handy, B.N., Acton, L.W., Kankelborg, C.C., Wolfson, C.J., Akin, D.J., Bruner, M.E., *et al.*: 1999, *Solar Phys.* **187**, 229. ADS. DOI.
Hansen, P.C., Pereyra, V., Scherer, G.: 2012, *Least Squares Data Fitting with Applications*, Johns Hopkins University Press, Baltimore, 163.
Ikhsanov, R.N., Marushin, Y.V.: 2003, arXiv. ADS.
Ikhsanov, R.N., Marushin, Yu.V., Ikhsanov, N.R.: 2004, In: Stepanov, A.V., Benevolenskaya, E.E., Kosovichev, A.G. (eds.) *Multi-Wavelength Investigations of Solar Activity*, *IAU Symp.* **223**, 257. ADS. DOI.

Ishii, T.T., Kurokawa, H., Takeuchi, T.T.: 1998, *Astrophys. J.* **499**, 898. ADS.
Jin, C.L., Qu, Z.Q., Xu, C.L., Zhang, X.Y., Sun, M.G.: 2006, *Astrophys. Space Sci.* **306**, 23. ADS. DOI.
Jing, J., Song, H., Abramenko, V.I., Tan, C., Wang, H.: 2006, *Astrophys. J.* **644**, 1273. ADS. DOI.
Joshi, B., Joshi, A.: 2004, *Solar Phys.* **219**, 343. ADS. DOI.
Künzel, H.: 1960, *Astron. Nachr.* **285**, 271. ADS.
Kurokawa, H.: 1987, *Solar Phys.* **113**, 259. ADS. DOI.
Kurokawa, H., Wang, T., Ishii, T.T.: 2002, *Astrophys. J.* **572**, 598. ADS. DOI.
Leka, K.D., Canfield, R.C., McClymont, A.N., van Driel-Gesztelyi, L.: 1996, *Astrophys. J.* **462**, 547. ADS. DOI.
Linton, M.G., Fisher, G.H., Dahlburg, R.B., Fan, Y.: 1999, *Astrophys. J.* **522**, 1190. ADS. DOI.
Livingston, W.: 2002, *Solar Phys.* **207**, 41. ADS. DOI.
López Fuentes, M.C., Mandrini, C.H.: 2008, *Bol. Asoc. Argent. Astron.* **51**, 31. ADS.
López Fuentes, M.C., Demoulin, P., Mandrini, C.H., van Driel-Gesztelyi, L.: 2000, *Astrophys. J.* **544**, 540. ADS. DOI.
Luoni, M.L., Démoulin, P., Mandrini, C.H., van Driel-Gesztelyi, L.: 2011, *Solar Phys.* **270**, 45. ADS. DOI.
Magara, T.: 2011, *Publ. Astron. Soc. Japan* **63**, 417. ADS. DOI.
Magara, T.: 2014, *Publ. Astron. Soc. Japan* **66**, L6. ADS. DOI.
Magara, T., Longcope, D.W.: 2003, *Astrophys. J.* **586**, 630. ADS. DOI.
Moffatt, H.K., Ricca, R.L.: 1992, *Proc. Roy. Soc. London A* **439**, 411. DOI.
Nishizuka, N., Asai, A., Takasaki, H., Kurokawa, H., Shibata, K.: 2009, *Astrophys. J. Lett.* **694**, L74. ADS. DOI.
November, L.J., Simon, G.W.: 1988, *Astrophys. J.* **333**, 427. ADS. DOI.
Park, J., Moon, Y.-J., Gopalswamy, N.: 2012, *Astrophys. J.* **750**, 48. ADS. DOI.
Petrovay, K., Moreno-Insertis, F.: 1997, *Astrophys. J.* **485**, 398. ADS.
Petrovay, K., van Driel-Gesztelyi, L.: 1997, *Solar Phys.* **176**, 249. ADS. DOI.
Pevtsov, A.A., Longcope, D.W.: 1998, *Astrophys. J.* **508**, 908. ADS. DOI.
Poisson, M., López Fuentes, M., Mandrini, C.H., Demoulin, P., Pariat, E.: 2013, *Adv. Space Res.* **51**, 1834. ADS. DOI.
Priest, E.: 2014, *Magnetohydrodynamics of the Sun*, Cambridge University Press, Cambridge, 270. ADS.
Ricca, R.L.: 1995, *J. Phys. A, Math. Gen.* **28**, 2335. ADS. DOI.
Rust, D.M., Kumar, A.: 1996, *Astrophys. J. Lett.* **464**, 199. ADS. DOI.
Sammis, I., Tang, F., Zirin, H.: 2000, *Astrophys. J.* **540**, 583. ADS. DOI.
Scherrer, P.H., Bogart, R.S., Bush, R.I., Hoeksema, J.T., Kosovichev, A.G., Schou, J., *et al.*: 1995, *Solar Phys.* **162**, 129. ADS. DOI.
Shi, Z.X., Wang, J.X.: 1994, *Solar Phys.* **149**, 105. ADS. DOI.
Shimizu, T.: 1995, *Publ. Astron. Soc. Japan* **47**, 251. ADS.
Shimojo, M., Shibata, K.: 1999, *Astrophys. J.* **516**, 934. ADS. DOI.
Solanki, S.K.: 2002, *Astron. Nachr.* **323**, 165. ADS. DOI.
Tanaka, K.: 1975, BBSO Preprint No. 0152, Big Bear Solar Observatory.
Tanaka, K.: 1991, *Solar Phys.* **136**, 133. ADS. DOI.
Tian, L., Alexander, D., Liu, Y., Yang, J.: 2005, *Solar Phys.* **229**, 63. ADS. DOI.
Török, T., Berger, M.A., Kliem, B.: 2010, *Astron. Astrophys.* **516**, 49. ADS. DOI.
van Driel-Gesztelyi, L., Malherbe, J.-M., Démoulin, P.: 2000, *Astron. Astrophys.* **364**, 845. ADS.
van Driel-Gesztelyi, L., Petrovay, K.: 1990, *Solar Phys.* **126**, 285. ADS. DOI.
van Driel-Gesztelyi, L., Csepura, G., Schmieder, B., Malherbe, J.-M., Metcalf, T.: 1997, *Solar Phys.* **172**, 151. ADS. DOI.
Waldmeier, M.: 1955, *Ergebnisse und Probleme der Sonnenforschung*, Geest & Portig, Leipzig, 164. ADS.
Yan, X.-L., Qu, Z.-Q., Xu, C.-L., Xue, Z.-K., Kong, D.-F.: 2009, *Res. Astron. Astrophys.* **9**, 596. ADS. DOI.
Zirin, H., Liggett, M.A.: 1987, *Solar Phys.* **113**, 267. ADS. DOI.
Zwaan, C.: 1978, *Solar Phys.* **60**, 213. ADS. DOI.